Modelling the effects of the radiation reaction force on the interaction of thin foils with ultra-intense laser fields

M J Duff[1], R Capdessus[1], D Del Sorbo[2], C P Ridgers[2], M King[1] and P McKenna[1]

[1]SUPA, Department of Physics, University of Strathclyde, Glasgow, G4 0NG, UK
[2]York Plasma Institute, Department of Physics, University of York, YO10 5DQ, UK

E-mail: matthew.duff@strath.ac.uk, remi.capdessus@strath.ac.uk, paul.mckenna@strath.ac.uk

October 2017

Abstract. The effects of the radiation reaction (RR) force on thin foils undergoing radiation pressure acceleration (RPA) are investigated. Using QED-particle-in-cell simulations, the influence of the RR force on the collective electron dynamics within the target can be examined. The magnitude of the RR force is found to be strongly dependent on the target thickness, leading to effects which can be observed on a macroscopic scale, such as changes to the distribution of the emitted radiation and the target dynamics. This suggests that such parameters may be controlled in experiments at multi-PW laser facilities. In addition, the effects of the RR force are characterized in terms of an average radiation emission angle. We present an analytical model which, for the first time, describes the effect of the RR force on the collective electron dynamics within the 'light-sail' regime of RPA. The predictions of this model can be tested in future experiments with ultra-high intensity lasers interacting with solid targets.

Keywords: Radiation reaction force; Radiation pressure acceleration; Relativistic laser-plasma interactions
Submitted to: *Plasma Phys. Control. Fusion*

1. Introduction

The multi-petawatt (PW) laser facilities currently under construction, such as the Extreme Light Infrastructure (ELI) [1] and APOLLON [2], will produce peak laser intensities exceeding 10^{23} Wcm^{-2}. It is expected that this will result in the acceleration of ions to energies of the order of hundreds of MeV per nucleon [3, 4, 5]. These high energies are expected to be produced by the radiation pressure of the ultra-intense laser light on the thin foil target; the so-called radiation pressure acceleration (RPA) mechanism

[6]. The transfer of momentum to the target as the laser reflects off its front surface can accelerate the target ions to high energies in quasi-monoenergetic bunches. The potential applications of the resulting beams of energetic ions include oncology [7] and the fast ignition approach to inertial confinement fusion [8, 9]. The effectiveness of the RPA mechanism is highest for targets which are just above the critical density (at which the plasma frequency is equal to the laser frequency) and is greatly reduced if the target undergoes relativistic self induced transparency (RSIT; caused by a reduction in the plasma frequency to below the laser frequency, due to the relativistic increase in the mass of the oscillating target electrons). Not only does the resultant laser propagation into the target volume reduce the radiation pressure on the surface, but it also heats the electrons in the bulk of the target, which enhances other acceleration mechanisms [10, 11, 12, 13]. The maximum ion energies which can be achieved using multi-PW laser systems may however be restricted by the onset of the radiation reaction (RR) force and QED effects (such as electron positron pair-production and stochastic photon emission), which become important at laser intensities exceeding 10^{22} Wcm^{-2} [14].

RR is the process by which electrons accelerating in ultra-intense laser fields experience a recoil force, due to momentum loss during radiation emission [15, 16, 17, 18]. This classical view of RR as a frictional force acting on the electrons has recently been demonstrated experimentally [19, 20, 21]. Above intensities of the order of 10^{22} Wcm^{-2} however, RR cannot be described classically, but instead must be described in the context of strong field QED. The importance of these QED effects are parameterized by χ_e, the ratio of the electric field strength experienced by the electron in its rest frame, to the QED field limit [22]. Quantum processes become important for $\chi_e \gtrsim 0.1$, with prolific pair production occuring at $\chi_e \simeq 1$. This parameter is strongly dependent on the interaction geometry; electrons which counter-propagate against a laser pulse experience Doppler-upshifted fields, leading to a higher χ_e and stronger RR. Radiation reaction has important consequences for experiments at future multi-PW laser facilities, as it not only affects the target electron dynamics, but also impacts on ion acceleration through modification to the self-consistent charge-separation fields within the plasma [23, 24]. The effects of RR on ion acceleration in the light-sail (LS) regime of RPA [25, 26] have been investigated in references [27, 28, 29, 30]. These studies indicate that it is the electrons which counter-propagate with respect to the laser pulse (and which are therefore subjected to the highest χ_e values) which experience significant RR effects in this regime.

In this article, we demonstrate via an analytical model that radiative cooling and reflection of electrons by the laser pulse changes the collective dynamics of the system. These RR effects manifest themselves in the distribution of radiation emitted from the target, in the energy partition between plasma species, and in the target dynamics. The model presented enables the photon conversion efficiency and the target velocity, which is reduced due to the influence of the RR force, to be calculated and verified against the predictions of QED-PIC (Particle-In-Cell) code simulations. To our knowledge, this is the first model describing such effects in the LS regime.

The remainder of the article is organized as follows. A brief overview of the underpinning theory of ultra-intense laser plasma interactions is presented in section 2. An analytical model which describes LS acceleration in the presence of the RR force is introduced in section 3. In section 4, a brief overview of the theory underpinning QED-PIC code simulations of high field interactions is provided, including the implementation of RR effects. The results of a series of 1D(3P) QED-PIC code simulations, investigating the radiation distribution, energy partition and target dynamics in the LS regime, are discussed in section 5. The simulation results are compared with predictions of the analytical model. The article concludes with a brief discussion of how the model predictions could be tested experimentally at multi-PW laser facilities.

2. Underpinning theory

2.1. Electron motion in strong fields

Electrons oscillating in ultra-intense laser fields can acquire relativistic velocities. The electron motion becomes relativistic when the dimensionless laser vector potential $a_0 > 1$ [31], where:

$$a_0 = \frac{eE}{m_e c \omega_L}, \tag{1}$$

e and m_e are the electron charge and mass, respectively, E is the electric field strength, c is the speed of light and ω_L is the laser frequency. Accelerating electrons in ultra-intense laser fields produce photons of radiation, which carry away momentum. This loss of momentum can be interpreted in the classical framework as a frictional force acting on the electrons, which is the RR force. The equation of motion for a radiating electron therefore depends on both the force from the external laser fields and the back-reaction force exerted due to the emission of high energy radiation from the relativistic electrons. For $a_0 \gg 1$, the photon formation length is small, in which case the emitted radiation is synchrotron-like. The spectrum can be described by the quantum synchrotron spectrum, with the radiation emitted into a narrow cone along the direction of electron momentum [32].

Provided that the magnitude of the RR force acting on the electron in its rest frame is much weaker than that of the Lorentz force, then the Landau-Lifshitz (LL) [16] model, which has been shown to be consistent with the classical limit of strong-field QED [33, 34], is sufficient to describe the electron dynamics. Treating RR as a frictional force, the LL equation can be expressed in vectorial form, as:

$$\frac{d}{dt}\mathbf{p}_e = \mathbf{F}_{L,e} + \mathbf{F}_{rad} \tag{2}$$

where, $\mathbf{F}_{L,e}$ is the Lorentz force, due to the external laser fields, and $\mathbf{F}_{rad}$ is the force exerted on the electron due to photon emission, which is related to the electron radiated power, P_γ, through the expression $\mathbf{F}_{rad} = -\frac{P_\gamma}{c}\boldsymbol{\beta}_e$.

We can write the electron radiated power in terms of the Lorentz force and a characteristic angle, such that:

$$P_\gamma = \frac{\tau_r \gamma_e^2}{m_e} \mathbf{F}_{L,e}^2 \Big(1 - \beta_e^2 \cos^2 \psi\Big) g(\chi_e). \tag{3}$$

Here, $\tau_r = \frac{e^2}{6\pi\epsilon_0 m_e c^3} \simeq 6.2 \times 10^{-24}$ s is the classical radiation time scale, corresponding to 2/3 times the light crossing time of the classical electron radius, and $\gamma_e = (1 - \beta_e^2)^{-1/2}$ is the Lorentz factor. The characteristic angle, ψ, which appears in equation (3) is the angle between the perpendicular component of the Lorentz force and the electron motion. χ_e is a Lorentz invariant parameter which describes the importance of quantum effects. These effects lead to an over-estimation of the electron radiated power in the semi-classical regime, and are accounted for through the introduction of a scaling factor, $g(\chi_e)$. Further details are provided in the Appendix. The quantum parameter is defined as follows:

$$\chi_e = \frac{\gamma_e}{e E_{sh}} \sqrt{\mathbf{F}_{L,e}^2 - (\mathbf{F}_{L,e} \cdot \boldsymbol{\beta})^2} \tag{4}$$

where, E_{sh} is the Schwinger limit for electric field strength, such that $E_{sh} = m_e^2 c^3 / e\hbar$ [22].

It is convenient to re-write the Lorentz force term in terms of the laser a_0, which is proportional to the intensity, and in terms of a characteristic angle, θ, which represents the projection of the electron velocity along the direction of laser propagation. We assume that the laser electric field has a larger magnitude than that of the charge separation field, such that $E_y \gg E_x$. This leads to the following expression for the Lorentz force:

$$\mathbf{F}_{L,e}^2 = a_0^2 (m_e c \omega_L)^2 (1 - \beta_e \cos\theta)^2. \tag{5}$$

We stress that the angles θ and ψ are not independent, as both depend on the electron momentum. Assuming that E_z is negligible, the relation between the angles is written:

$$\cos\psi = \frac{\alpha \cos\theta + \sin\theta}{\sqrt{1 + \alpha^2}}. \tag{6}$$

where $\alpha = E_x / E_y$, such that when $E_y \gg E_x$, $\psi \simeq \frac{\pi}{2} - \theta$. Using these equations, it is now possible to evaluate the force exerted on an electron due to photon emission:

$$\mathbf{F}_{rad} = g(\chi_e) \mathcal{G}(\theta) \boldsymbol{\beta}_e \tau_r \omega_L \gamma_e^2 a_0^2 m_e c \omega_L. \tag{7}$$

We have introduced a function, $\mathcal{G}(\theta)$, into equation (7) which gathers the terms relating to the angular dependence of the electron radiated power. This function is written explicitly below.

$$\mathcal{G}(\theta) = \frac{(1 - \cos\theta)^2}{1 + \alpha^2} \Big(1 + \alpha^2 - (\alpha \cos\theta + \sin\theta)^2\Big) \tag{8}$$

3. Modelling the radiation losses

Radiation reaction effects are typically overlooked in the LS regime of radiation pressure acceleration; since the targets can acquire relativistic velocities, the laser fields are strongly Doppler shifted, reducing the intensity which arrives at the target in its reference frame. This effect has been observed in a recent study by Del Sorbo *et al* [35], in which quantum effects are found to be quenched due to the high target velocity which can be obtained in the LS regime. That study used circularly polarized laser pulses, in which case electron heating via the oscillating component of the ponderomotive force is suppressed, and the targets undergo highly efficient acceleration. By contrast, here we consider linear polarization such that the electron heating effects are still present, allowing RR to influence the collective electron dynamics.

Whilst RR effects are negligible when the target acts as a perfectly reflecting mirror, as previously described, it is not the case for this study, where the target can instead absorb laser energy. Ionization of the target front surface produces a plasma, in which the electrons gain energy from the laser, and subsequently experience radiative cooling as they oscillate in the strong electromagnetic fields. These radiating electrons are found to be localized to within the target charge depletion zone. The cooling of electrons through the RR force changes the dynamics of the self-consistent fields within the target, therefore impacting the ion dynamics [36, 28, 29]. As the target continues to absorb laser energy it will expand, resulting in a decrease in the electron density. When the target areal density, ξ, reaches the same order of magnitude as the laser a_0, it can undergo relativistic self induced transparency (RSIT), at which point the electrons in the bulk of the target are strongly heated and the efficiency of target acceleration is greatly reduced. The normalized areal density for a target of thickness, l, and with a critical density n_c, is given by $\xi = \pi \frac{n_e}{n_c} \frac{l}{\lambda_L}$ [26, 25].

We have outlined various scenarios in which the RR force can have a significant effect on the collective electron dynamics within the LS regime. In order to model these effects, we present a modification to an existing LS model, which is detailed in Macchi *et al* [25].

An intense laser pulse interating with a solid target can be reflected, absorbed, or transmitted (if the target undergoes transparency during the interaction). The relative probabilities of these outcomes are related as follows:

$$\mathcal{R} + \mathcal{T} + \mathcal{A} = 1 \tag{9}$$

where $\mathcal{R}, \mathcal{T}$ and $\mathcal{A}$ represent, respectively, the reflection, transmission and absorption coefficients. The existing LS equation of motion accounts only for reflection of laser light off the target. However, the case which we present here allows for laser light to be absorbed. We begin by assuming no transmission, such that $\mathcal{T} = 0$, since the target is initially overdense and we only consider the collective electron dynamics up until the time of transparency. The target reflectivity can then be expressed uniquely as a

function of absorption ($\mathcal{R} = 1 - \mathcal{A}$), leading to the following equation of motion:

$$\frac{d}{dt}(\gamma_t \beta_t) = \frac{I}{\rho l c^2}(2 - \mathcal{A})\frac{1 - \beta_t}{1 + \beta_t}. \tag{10}$$

The absorption term is obtained by normalizing the intensity of radiation emitted by the electrons, up until the target undergoes transparency (at time $t = t_{tr}$), to the laser intensity

$$\mathcal{A} \approx \frac{N_{rad} \int_0^{t_{tr}} \langle P_\gamma \rangle dt}{\int_0^{t_{tr}} I_L dt} \tag{11}$$

where,

$$\langle P_\gamma \rangle \equiv \frac{\int_{\mathbb{R}^3} f_e P_\gamma d\mathbf{p}_e}{n_e}, \tag{12}$$

is the total radiated power of the electrons of the plasma, such that $n_e \equiv \int_{\mathbb{R}^3} f_e d\mathbf{p}_e$ defines the electron number density.

In order to evaluate the total radiated power, we require knowledge of the radiating electron distribution function. Assuming that electrons are strongly heated by the oscillating component of the ponderomotive force, which is particularly true in our study due to the use of linear laser polarization, the electron distribution is modelled using an isotropic Maxwell Juttner distribution such that

$$f_e(\gamma_e) = \mathcal{N} \exp\left(-\frac{(\gamma_e - 1)}{\Theta}\right) \tag{13}$$

where, $\mathcal{N} = \frac{n_e}{4\pi m_e^3 c^3 K_2(1/\Theta)\Theta}$ is the normalization coefficient and $\Theta = \frac{T_e}{m_e c^2}$. Since $a_0 \gg 1$ we may assume $T_e \sim a_0 m_e c^2$ which yields

$$\langle P_\gamma \rangle = 12 a_0^4 \mathcal{G}(\theta)\, g(\chi_e)\, \omega_L \tau_r m_e c^2 \omega_L. \tag{14}$$

We have used that $K_2(1/\Theta) \simeq 2\theta^2$ for $\Theta \gg 1$ and assumed $\beta_e \simeq 1$ in the functions $\mathcal{G}(\theta)$ and $g(\chi_e)$. Comparison with electron spectra obtained from simulations, however, indicates that whilst the Maxwell Juttner distribution is a reasonable approximation (further details are provided in the Appendix), it overestimates the electron temperature. To account for this, we introduce a scaling function analogous to that described in reference [37], which describes the cooling of the electrons.

$$\mathcal{S}(\theta, \phi) = 1 + \omega_L \tau_r \mathcal{G}(\theta) a_0^3 \int_0^{\phi} \varphi^2(\phi') d\phi' \tag{15}$$

where φ is a function describing the pulse shape and $\phi = kx - \omega_L t$ is the phase. This scaling is applied in the evaluation of equation (11).

The number of radiating electrons per unit surface, N_{rad}, can be estimated from the dynamic hole boring picture of RPA. Here, the laser radiation pressure accelerates a compressed layer of electrons, leaving behind a region of charge depletion. This results in the formation of a charge separation field, which subsequently accelerates the target ions until they catch up to the electrons. At this point, charge balance is restored and the electrons can propagate back into the depletion zone. These electrons counter-propagate with respect to the laser and therefore experience strong RR. The physics

described in this picture is similar to the physics of the radiating electrons in the LS regime. Figure 4 further illustrates the similarities, and demonstrates how, in this study, radiation emission is localized to the target depletion zone, i.e. the distance over which the charge separation field extends.

Liseykina *et al* [38] derive an expression for the number of radiating electrons in the hole boring regime, under the assumption that $a_0 n_c/n_0 > 1$, with $n_c = \sqrt{\gamma_e \epsilon_0 m_e \omega_L^2/e^2}$ representing the critical density. This leads to an expression for N_{rad} which is independent of the target thickness. This is not the case for the simulations presented here; instead we derive an expression for N_{rad} which is dependent on the size of the charge depletion zone, and therefore on the overall target thickness. Following the method outlined in reference [38], we balance the electrostatic pressure with laser radiation pressure, in this case eliminating the skin depth from the resulting equations to derive the following expression:

$$N_{rad} = \frac{a_0^2}{\pi}\frac{n_c}{n_0}\frac{1}{r_c d}\Big(\Big(\frac{1}{4}+\frac{1}{4}\Big(\frac{n_0 d\omega_L}{n_c c a_0}\Big)^2\Big)^{1/2}-\frac{1}{2}\Big). \tag{16}$$

Here, $r_c = e^2/m_e c^2$ is the classical electron radius, n_0 is the initial electron density in the target skin depth, and d is the size of the charge depletion zone, indicating the region where radiation production is localized. In the case where $a_0 n_c/n_0 > 1$, the scaling derived in reference [38] is obtained, namely

$$N_{rad} = \frac{a_0}{r_c \lambda_L}. \tag{17}$$

Equation (17) assumes that the target, in the hole boring regime, is infinitely thick. A return current can therefore be drawn to cancel the charge separation field, allowing electrons to return to the charge depletion zone and produce radiation as they counter-propagate with respect to the laser. In the LS regime however, the targets are significantly thinner, meaning that a smaller return current is drawn and therefore the number of radiating electrons is reduced. The size of the depletion zone clearly impacts the number of radiating electrons. Equation (16) accounts for this target thickness dependence, predicting a smaller number of radiating electrons compared to (17) in the range of thickness considered here.

Finally, using equation (17), an estimate of the absorption can be obtained:

$$\mathcal{A} \approx \frac{a_0^3}{r_c \lambda_L}. \tag{18}$$

In our case however, the absorption remains a more complicated function of a_0, obtained by substituting equations (12) and (16) into (11). The absorption, equivalent to the photon conversion efficiency, calculated by this model is plotted in figure 5. It can be seen that there is good qualitative agreement with the values calculated from the simulations.

The target velocity can subsequently be re-derived, by substituting the approximation for the absorption into the modified equation of motion and integrating with respect to time. Following the method of reference [39], we change variable to the

phase, ϕ, and integrate up to the time of transparency, at which point the efficiency of the RPA will be greatly reduced. This leads to an expression for the target velocity of the following form:

$$\beta_t = \frac{(\epsilon(\phi) - a(\phi) + 1)^2 - 1}{(\epsilon(\phi) - a(\phi) + 1)^2 + 1}. \tag{19}$$

where $\epsilon(\phi) = 2F(\phi)/\rho l c^2$ is the normalized laser fluence, such that $F(\phi) = \int_0^\phi I(\phi')d\phi'$ and $a(\phi = \phi_{tr})$ is the radiative correction evaluated at the time at which the target undergoes transparency, given by

$$a(\phi = \phi_{tr}) = 12\mathcal{G}(\theta)g(\chi_e)\frac{\omega_L^2 \tau_r m_e c^2 \int_0^{\phi_{tr}} a_0^5(\phi')d\phi'}{r_c \lambda_L \rho l c^2}. \tag{20}$$

When the conversion of laser energy to photons is negligible, i.e. for a model which neglects RR, the expression for the target velocity derived in reference [25] is recovered.

4. Numerical approach

4.1. Numerical model

PIC codes offer a good description of collisionless plasmas where collective effects dominate. Within the plasma, the emission of synchrotron radiation from relativistic electrons is handled stochastically, using a Monte-Carlo algorithm to compute the probability of photon emission. The synchrotron photons correspond to high-frequency radiation, in which case the interaction of photons, electrons and positrons is handled using the method of Baier and Katkov [40]. The emitted photons carry away momentum, which is subtracted from the classical momentum of the radiating particle. The particles therefore follow a classical trajectory between photon emission events. Stochastic effects (described in detail in the Appendix) are accounted for in this way, rather than through the damping of the RR term in the LL equation.

In the simulations presented in this paper, we isolate effects which arise purely due to RR by running simulations with and without RR. In the cases with RR off, photons of synchrotron radiation are still produced, however there is no subsequent recoil force on the electrons. This situation is unphysical, and is only used as a tool to extract the physics which arises due to purely RR effects.

4.2. Simulation parameters

We present the results of 1D(3P) simulations using the fully relativistic EPOCH QED PIC code [41]. 1D simulations have been used to scan over a wide range of parameters with high resolution. We investigate the interaction of solid density ($777n_c$, which is also initially relativistically overdense, such that $n_e > \gamma n_c$) aluminium targets, in a charge state of 13^+, with an ultra-intense Gaussian laser pulse with a peak intensity of $2{\times}10^{23}$ Wcm^{-2} (corresponding to a peak $a_0 = 382$). The pulse has a wavelength of 1μm and

a FWHM pulse duration of 60 fs. Initially the simulations have 1000 particles-per-cell and a spatial resolution of 2 nm, leading to a high spatial convergence.

At the intensity considered, the RR force will play a role in the electron dynamics whilst higher order QED effects such as pair-production can be neglected [42]. The quantum parameter, χ_e, is small in this regime however we re-iterate that the stochastic effects associated with a small but non-negligible value of χ_e are accounted for in the Monte-Carlo algorithm for photon emission.

The targets are varied in thickness in the range l=50-400 nm, such that during the interaction they are accelerated in a LS like regime. In order to be rigorous, we refer in this paper to a LS like regime, as some of the assumptions used in the derivation of the LS model presented in reference [25] do not hold. For example, in this case the target does not act like a perfect mirror as some of the laser energy is absorbed, and the RR force will change the dynamics of the system.

We consider only linear polarization here, in contrast to the recent study by Del Sorbo *et al* [35]. This choice accentuates the RR effects, due to an enhancement in the electron heating through the oscillating component of the laser ponderomotive force. The enhancement to RR effects in linear polarization has been reported in references [6, 29]. In addition, the use of linearly polarized light makes this study more relevant for the guidance of future experiments. The first experiments on ELI-NP, for example, are likely to use linear polarization as only one of the two 10 PW beams will be initially commissioned with control over the laser polarization [43].

5. Numerical simulations results

5.1. Distribution of emitted radiation

The effect of the RR force acting on the collective electron dynamics can be quantified through changes in the distribution of the emitted radiation from the target. In order to characterize these changes, we define a first average emission angle by taking the ratio of the electron transverse to longitudinal momentum and averaging over the electron distribution function, as follows:

$$\langle\theta\rangle = \frac{\int_{\mathbb{R}^3} \theta f_e \mathbf{dp}_e}{\int_{\mathbb{R}^3} f_e \mathbf{dp}_e} \tag{21}$$

$$\theta \quad = \arctan\left(p_{e,y}/p_{e,x}\right). \tag{22}$$

Here, the output angles are in the range $\langle\theta\rangle \in [-\pi, \pi]$, with $\pi/2$ the direction perpendicular to target normal. In this section, radiation emitted in the 'backwards' direction is taken to mean emission at angles $\mid \langle\theta\rangle \mid \in [\pi/2, \pi]$.

In the calculation of the average emission angles, it is possible to use the electron momentum to infer information about the distribution of radiation. This is due to the high average electron energies involved. As discussed in equation (A.1), the synchrotron radiation is oriented along the direction of electron momentum and emitted into a cone

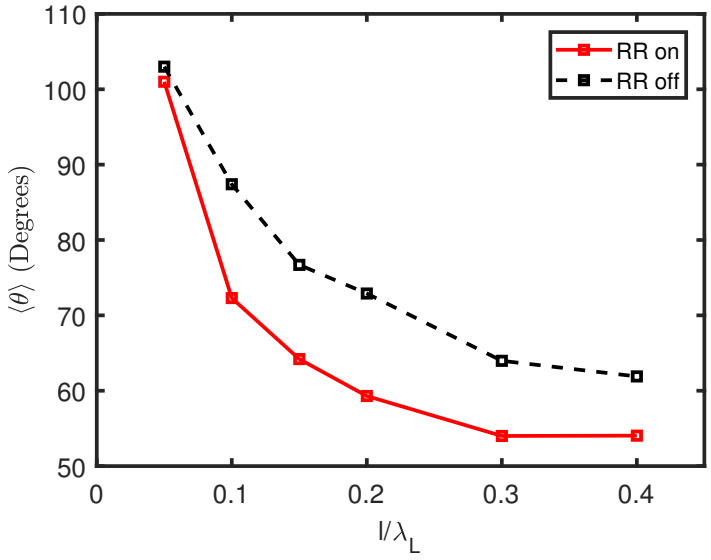

Figure 1. Average emission angle $\langle\theta\rangle$ as a function of target thickness, calculated at the time of maximum synchrotron emission. The solid red line represents the case with RR on, whilst the dashed black line is the case with RR off.

with an opening angle equal to $1/\gamma_e$. Therefore the direction of an emitted photon is assumed to be the same as that of the emitting electron, correlating the electron and photon average emission angle and allowing these to be used interchangably.

Figure 1 shows the first average emission angle as a function of target thickness, with and without RR. We remind the reader that without RR, photons of synchrotron radiation are still produced, however their momentum is not accounted for and the electron does not experience a recoil force. This case is included only to give an indication of how the RR force changes the collective electron dynamics. Each point in figure 1 is calculated at the time of maximum synchrotron emission for the corresponding target thickness.

Figure 1 shows a decrease in the average emission angle for the case with RR on, caused by radiative cooling and reflection of the electron population which moves against the laser. As discussed in section 3, this electron population is formed as the target front surface ionizes, producing an expanding plasma. The plasma electrons which propagate in the backwards direction then experience the strongest RR effects due to a Doppler upshift of the laser fields, to the point where they can be reflected by the pulse. These electrons can no longer contribute radiation in the backwards direction, therefore causing a decrease in the average emission angle.

From figure 1, it can be seen that the average emission angle depends on the target thickness. For the thinnest targets, transparency occurs early during the interaction, producing an expanding plasma. The plasma electrons within the laser focal spot are ejected by the ponderomotive force and therefore interact with a lower intensity, resulting in weak RR effects. As the target thickness increases, RR significantly changes

the charge separation fields within the plasma, leading to a reduction in the average emission angle with RR on. For these target thicknesses, there is a higher number of radiating electrons, meaning that more will be cooled and reflected by the laser. These electrons bunch up at the laser plasma interface, producing a region of high electron density and therefore increasing the strength of the charge separation fields within the target. This allows the electrons to acquire a larger longitudinal momentum and therefore, as p_x increases, the average emission angle decreases. This increase in the magnitude of the charge separation fields only occurs with RR on, since it is related to the cooling and reflection of the electrons by radiation emission. The number of radiating electrons is maximized for a target thickness of 200 nm, in agreement with the N_{rad} calculated using equation (16). This is also the thickness which corresponds to the largest reduction in average emission angle, with and without RR. For the thickest targets however, the areal density is sufficiently high that the laser drives a strong electrostatic shock. The electrons therefore experience shock driven acceleration, leading to weaker RR effects.

The reduction in the average emission angle can be related to a change in the target velocity. Since the radiation is more forwards directed when RR effects are included, the emission of synchrotron photons will induce a larger recoil force on the target compared to the case with RR off. This occurs due to the smaller average emission angle, as there will be a larger component of the RR force along the direction of target propagation since this varies with the cosine of the emission angle.

An important point to consider here is that the model presented in section 3 applies only to targets where the electrons have radiated the majority of their energy before the target undergoes transparency, i.e. $t_{rad} < t_{tr}$. If this is not the case, then the effects of the RR force on the collective electron dynamics are washed out by the onset of transparency and RR effects are negligible. For the 50 nm case, this condition is not satisfied, and instead the maximum synchrotron emission time occurs after transparency. This explains why the average emission angle is $> \pi/2$, there are no significant RR effects to reflect the electrons and reduce the radiation emission in the backwards direction. We point out that whilst the average emission angle can be obtained from the photon spectra, and could potentially be measured in future experiments, that the condition $t_{rad} < t_{tr}$ may be necessary before macroscopic RR effects can be observed.

The effect of the RR force on the collective electron dynamics can be observed in the angular photon distribution. The angular distributions for a 50 nm target and a 200 nm target are compared in figures 2 (a) and (b) respectively. Both of these distributions are measured at the time of maximum synchrotron emission for the corresponding target. This figure further illustrates how the magnitude of the RR force is sensitive to the target thickness, therefore leading to significant changes in the photon distributions. Again, we stress that in the 50 nm case, transparency occurs before the maximum radiation emission time and therefore we can observe radiation emitted predominantly in the backwards direction. For thicker targets, in the regime where $t_{rad} < t_{tr}$, distinct lobes can be seen in the photon distributions.

The analysis of the emitted radiation has thus far shown that radiative cooling of

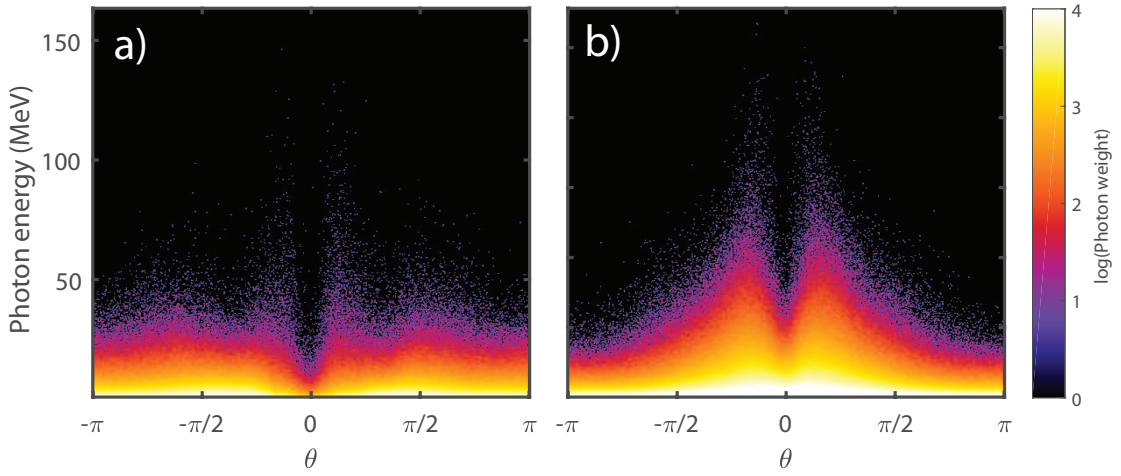

Figure 2. Photon angular distributions for (a) 50 nm target and (b) 200 nm target. These distributions are compared at the time of maximum synchrotron emission, corresponding to times $t = 13\ T_L$ and $t = 31\ T_L$ respectively.

electrons leads to a decrease in the average emission angle of the emitted radiation, an effect which can be observed in the photon distribution. We can develop this analysis further by defining a second average emission angle, $\delta\theta$, which quantifies differences in the distributions with and without RR. This angle is defined as follows:

$$\delta\theta = \arctan\left(\frac{\langle \delta p_y \rangle}{\langle \delta p_x \rangle}\right) \tag{23}$$

where,

$$\langle \delta p_x \rangle \equiv p_{x,RR\ on} - p_{x,RR\ off} = \int_0^t F_{rad,x}\left(t'\right) dt' \tag{24}$$

$$\langle \delta p_y \rangle \equiv p_{y,RR\ on} - p_{y,RR\ off} = \int_0^t F_{rad,y}\left(t'\right) dt' \tag{25}$$

leading to:

$$\delta\theta = \arctan\left(\frac{\int_0^t a_0^2(t')\beta_{e,y}\mathcal{G}(\theta)dt'}{\int_0^t a_0^2(t')\beta_{e,x}\mathcal{G}(\theta)dt'}\right). \tag{26}$$

The brackets $\langle\rangle$ indicate that we are subtracting the entire distribution with RR off from that with RR on. The argument of the arctan in equation (26) is the ratio of the impulse exerted by the RR force in the transverse direction compared to the longitudinal. The angle $\delta\theta$ therefore gives an indication of the partition of the RR force into each of these directions, and the subsequent contraction of phase space in each direction resulting from radiative cooling. For the target parameters considered in this article (i.e. strongly overdense targets), the contraction is too small to report any significant changes in the phase space distribution. This is confirmed by estimating the

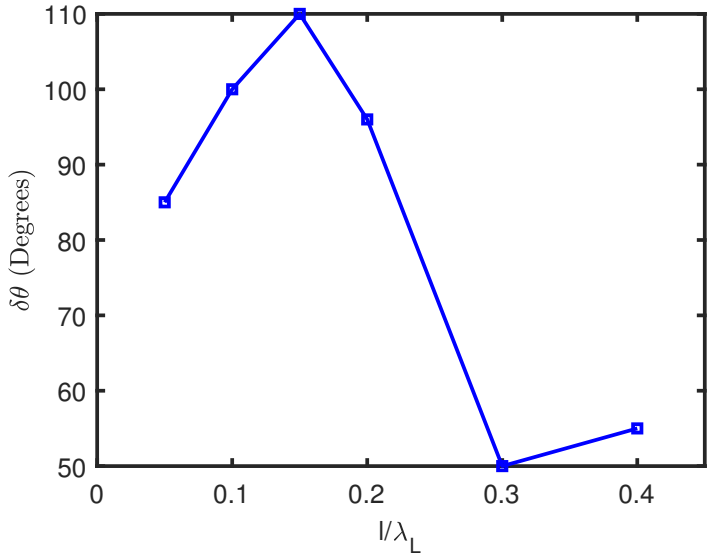

Figure 3. Variation of the second average emission angle, $\delta\theta$, with target thickness. This angle provides information on the partition of the RR force into the longitudinal and transverse directions.

amplitude of the contraction using equation (15). For the target parameters used in this study, the reduction in phase space volume is approximately a factor of 1.5.

An interesting feature of this second emission angle is that it is deterministic rather than stochastic. This can be seen in equation (26), where $\delta\theta$ is seen to depend on the integration over time of the laser intensity and the target velocity. It therefore maps out the history of the RR force during the interaction, rather than being a stochastic variable. It is found that $\delta\theta$ is the average emission angle which should be used to define $\mathcal{G}(\theta)$, since this angle quantifies the differences in the electron populations with and without RR. It is implied that after averaging over the distribution, $\langle\theta\rangle \to \delta\theta$.

The variation of the second average emission angle with target thickness is plotted in figure 3. For targets between 50-200 nm thick, we can see that the large values of the average emission angle ($\delta\theta \gtrsim \pi/2$) implies that $\delta p_y \gg \delta p_x$ and so there is more contraction of phase space in the transverse direction compared to that of the longitudinal. This difference again is an effect of the onset of transparency; as the targets undergo RSIT, an expanding plasma is produced in which the electrons are heated as they expand in the longitudinal and transverse directions. The comparatively thicker targets are not subject to this effect, and so the radiative cooling predominantly occurs for electrons returning to the charge depletion zone (i.e. a longitudinal effect).

The key point of these results is that the collective electron response to the RR force is sensitive to the target thickness, such that the collective effects can be quantified from the distribution of emitted radiation through an appropriate choice of average emission angle.

5.2. Energy partition and target dynamics

The dynamics of the target as it accelerates in the LS like regime are investigated in more detail in this section. Futher details of this regime are provided in figure 4. Radiation pressure from the laser pushes electrons in the target into the skin depth, the distance over which the laser fields evanescently decay within an overdense target. This forms a compressed layer of electrons, which is then pushed into the bulk of the target by radiation pressure. The charge imbalance as the electrons accelerate away from the ions produces a charge separation field, which subsequently accelerates the ions. The region of high electron density, and the resulting charge separation field, are plotted from a sample simulation in figure 4. As discussed in section 2, it is the counter-propagating electrons which experience the strongest RR; this effect is further illustrated in figure 4, where the spatial distribution of the electron radiated power is overlaid with the spatial distribution of the charge separation field. This figure indicates that radiation production is localized to within the charge separation field, enabling calculation of the number of radiating electrons using our analytical model.

The conversion efficiency of laser energy into plasma species has been investigated

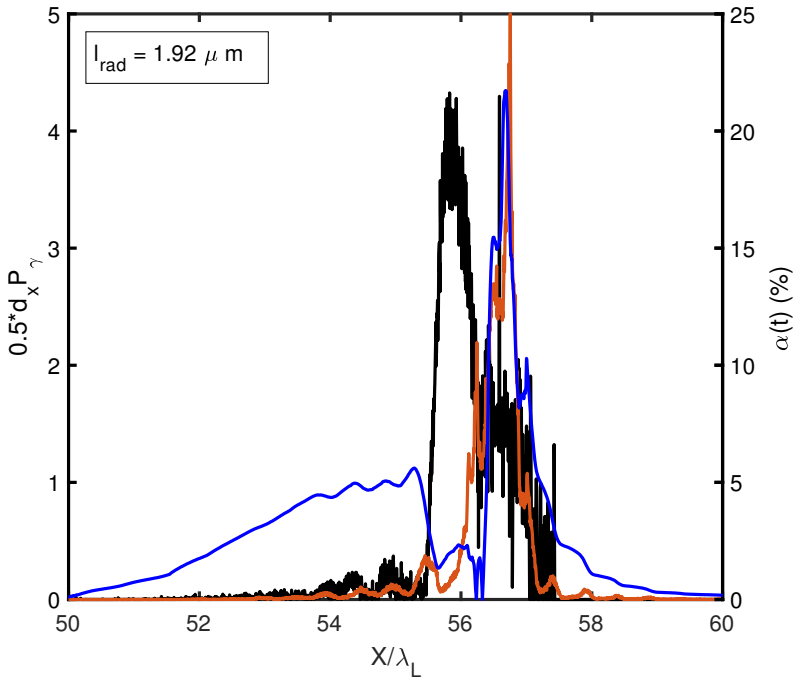

Figure 4. Diagram showing the dynamics of the LS like regime. This plot corresponds to the 150 nm target at the time of maximum radiation emission ($t_{rad} = 23\ T_L$). The blue line corresponds to the ratio of the magnitudes of the charge separation field to the laser field, such that $\alpha(t) = E_x(t)/E_y$. The spatial distribution of the electron radiated power is plotted in black, indicating that radiation is produced in the charge depletion zone. The ratio $n_e/\gamma_e n_c$, normalized to its maximum value, is plotted in red, showing that the charge separation field is generated in the electron depletion zone.

as a function of target thickness, with and without RR, in figure 5. We compare our results to a similar 1D(3P) simulation study by Tamburini *et al* [29], in which the energy partition was investigated as a function of time for a fixed target thickness. Similar laser and target parameters were used in the aforementioned study ($I = 2.33 \times 10^{23}$ Wcm^{-2} and $n_e = 100 n_c$).

A key feature of figure 5 is that the electron conversion efficiency remains relatively unchanged, with and without RR. Since RR causes the electrons to radiatively cool, it would be expected that the electron conversion efficiency would subsequently decrease. This effect can again be related back to the counter-propagating electrons, which are cooled and reflected by the laser and subsequently trapped at the laser plasma interface. Here, they can continue absorbing laser energy, approximately balancing the radiation losses.

Figure 5 shows that the ion conversion efficiency in ultra-intense laser solid

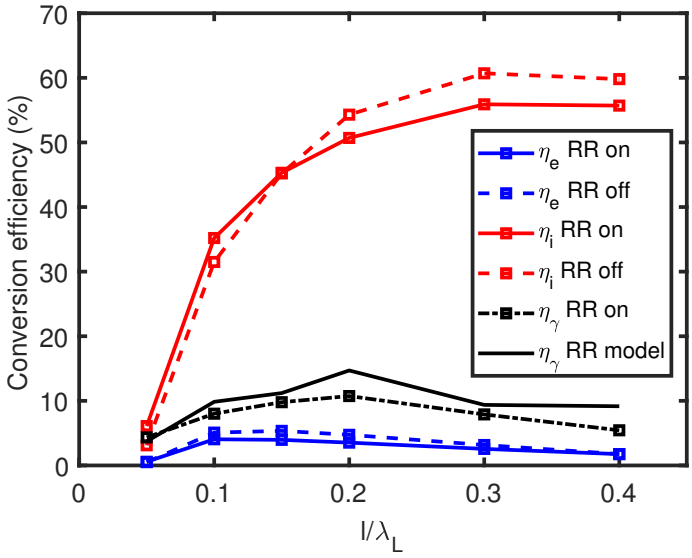

Figure 5. Conversion efficiency of laser energy to electrons (blue), ions (red) and photons (black). Dashed lines represent the cases with RR off, whilst solid lines indicate the cases with RR on. The photon conversion efficiency with RR off is omitted, as this does not conserve energy and therefore has no influence on the energy partition. The solid black line refers to the absorption calculated using our model, whilst the dot-dash black line is the photon conversion efficiency measured from simulations.

interactions is high (peaking around 60%), due to ion acceleration in the strong electrostatic fields within the target. In addition, the limitation of the simulations to 1D will result in an overestimation of the ion conversion efficiency, since the target does not undergo transverse expansion and the ions are pushed only along the laser axis. The ion conversion efficiency exhibits different behaviour throughout the range of target thicknesses investigated. For the thinnest targets, there is little difference between the cases with and without RR, due to early onset transparency reducing the impact of RR on the charge separation fields. However, for target thickness beyond 150 nm, a

reduction in the ion conversion efficiency occurs for the case with RR on. This is because more of the laser energy is converted into photons of synchrotron radiation. Since the electron conversion efficiency remains the same with and without RR, differences in the energy partition are a result of laser energy being coupled preferably into radiation as opposed to ions. With RR off, we do not consider the laser energy coupled into radiation, since this case does not conserve energy. The ion conversion efficiency is therefore higher as laser energy can only be shared between the ions and electrons, and as discussed earlier, the electron conversion efficiency is relatively unchanged with and without RR.

The photon conversion efficiency is shown in figure 5 for the case with RR on (dot-dashed black line). The magnitude of the photon conversion efficiency, as calculated from the simulations, is of the of order 10% and therefore in agreement with the results reported in reference [29]. The black solid line in figure 5 represents the photon conversion efficiency, calculated using our analytical model. There is good agreement with the simulation results, showing the same peak in photon conversion efficiency for a target thickness of 200 nm. This is the same case for which the number of radiating electrons is maximized, as predicted using our analytical model, equation (16). This model however tends to overestimate the photon conversion efficiency, as it does not account for transparency of the target and therefore the 'loss' of laser energy transmitted through the target.

Finally, we can use the simulations to verify the predictions of the target velocity from our analytical model. The target velocity is obtained from simulations by tracking the position of maximum electron density as a function of time. This maximum density surface indicates the interface at which RPA occurs.

Figure 6 compares the target velocity measured from the simulations (solid blue line) to the predictions of our analytical model (solid black line) using equation (19). We also compare our results to an existing LS model, which assumes the target is perfectly reflective (solid red line) as derived in reference [25]. This model acts as an upper bound for the target velocity; it is found to overestimate the target velocity in all cases, since many of the targets used in this study undergo transparency and therefore are not efficiently accelerated. It should be noted that LS acceleration is an idealized scenario, and in reality the target velocity can deviate from the LS predictions at various points in the interaction. We have compared the target velocity with the predictions of the hole-boring (HB) model [44], to ensure that we are operating close to perfect LS. The simulations show that for these targets, on average, the target velocity is close to the HB velocity for only the first 15 laser periods, after which point the target velocity rapidly increases beyond the predictions of the HB model and closely approximates LS. The target velocities from the models are calculated at the time of maximum synchrotron emission, in keeping with the assumptions made in our analytical model. The target velocity in the simulations increases more slowly with time, compared to the predictions of the models, finally tending towards the model predictions at later times. This is due to heating mechanisms which are important in the early stages of the interaction and

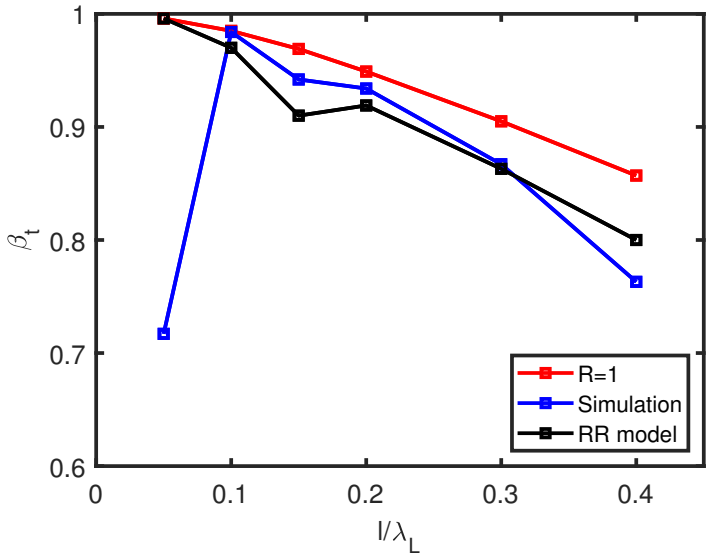

Figure 6. A plot comparing the target velocity predicted by our model (solid black line) to measurements from simulations (solid blue line) and an existing LS model (red solid line) which assumes the reflectivity of the target, $\mathcal{R}$, is unity.

which complicate the dynamics of the RPA process. For this reason, we measure the target velocity at the end of the simulation, when it has reached a constant value.

For the cases where the radiated power is high, we can obtain radiative corrections which are larger than the normalized fluence. This arises from the assumption that the electron temperature scales according to the ponderomotive potential. In order to correct for this, the radiative correction is scaled by the ratio $T_e(\phi_{rad})/T_e(\phi_0)$. Here, $T_e(\phi_{rad})$ is the electron temperature at the time of maximum synchrotron emission, and $T_e(\phi_0)$ is the electron temperature associated with the laser a_0 measured at this same time.

From figure 6, we see relatively good agreement between the velocity calculated using our RR model and the simulations. The agreement is better for thicker targets ($\xi > a_0$), where transparency is not as important in the dynamics. As our model does not account for transparency (only RR effects), this is to be expected. Our model tends to overestimate the reduction in target velocity, particularly in the cases where the radiated power is high (i.e. the 150 nm target, for which the function $\mathcal{G}(\theta)$ is maximized). The possibility remains that a model could be developed which produces better agreement for ultra-thin targets (<100 nm) by accounting for both RR and transparency effects. The reduction in target velocity reported here leads to lower ion energies, and may point towards less efficient RPA than predicted for future experiments. Understanding the underlying processes could however result in control over the radiation production, energy partition and target dynamics.

5.3. Experimental prospectives

We have presented a 1D analytical model which describes the effects of the RR force on collective electron dynamics within the LS regime. This enables calculation of the laser energy absorption and the velocity of the target as it undergoes radiation pressure acceleration. In deriving this model, we assume that the charge separation field, whilst not negligible, is weaker than the laser field, although it enhances the production of high energy radiation [45]. The role of the charge separation field is an important aspect of the model and one which could be investigated experimentally (for example, via measurements of ion acceleration).

The model can also be used to make qualitative predictions about the distribution of the emitted radiation, which could be tested in future experiments. A key feature, described in section 5.1, is that the angular emission decreases as a function of target thickness and that the rate of decrease changes due to RR. Experiments at multi-PW facilities could test this dependency (for example, by making angularly-resolved measurements of radiation emission, using arrays of scintillators, X-ray film or ImagePlate detector). Cyrogenic hydrogen targets could be used to reduce Bremsstrahlung emission, as discussed for example in references [43, 45].

Finally, in section 5.1 it is shown that the distribution of emitted radiation changes depending on the time at which relativistic transparency occurs during the interaction. In particular, we note the disappearance of lobe-like structures from the photon distribution if the interaction is transparency dominated. If this effect is experimentally verified, it may act as a diagnostic for the onset of the transparency process.

6. Conclusions

Building upon the work presented in references [28, 29], we have further demonstrated that semi-classical RR effects can be significant in the LS regime of RPA if the absorption of laser energy by target electrons is considered, rather than assuming the target acts as a perfect relativistic mirror, i.e when $a_0 > \xi$. By defining an average emission angle, the magnitude of the RR force effects on the collective electron dynamics can be characterized. We show that the amplitude of the RR force is determined by the target thickness, and investigate this effect over a wider range of target parameters than those presented in reference [24].

We present, for the first time, an analytical model that describes the response of the collective electron dynamics to the RR force in the LS regime. By accounting for the emitted radiation within the absorption coefficient (implying that the target acts as a non-perfect mirror), the model predicts the absorption of laser energy to photons and the resulting target velocity. Changes in the angular emission of radiation enable characterization of the transition into the relativistic self induced transparency regime.

The predictions of this model have been verified using QED PIC code simulations.

We have also outlined aspects of the model which can be experimentally tested at multi-PW laser facilities. This study indicates that the distribution of radiation from thin foils in ultra-intense laser solid interactions will provide fundamental insights into high-field plasma physics, where the collective plasma physics effects are intertwined with strong field QED effects.

Acknowledgments

This work was funded by the UK EPSRC (grant numbers EP/M018091/1, EP/R006202/1, EP/P007082/1 and EP/M018156/1). We also acknowledge the use of the EPOCH PIC code (developed under EPSRC grant EP/G054940/1) and both the Archie-WeST and ARCHER (EP/L000237/1) supercomputers in the running of the simulations presented here. Data associated with research published in this paper is accessible at http://dx.doi.org/10.15129/e7fda3c4-a5a4-47b4-a224-5d9b0aeaeb71.

Appendix A.1. The synchrotron radiation

In the case of an ultra-relativistic electron oscillating in a strong laser field, the synchrotron radiation is emitted into a narrow cone, pointing along the direction of the electron momentum[46]. For a single electron, the spectral intensity of the synchrotron radiation, per unit solid angle, is:

$$\frac{d^2 I_\gamma}{d\omega d\Omega} = \frac{P_\gamma}{\omega_{cr}} \delta(\mathbf{\Omega} - \mathbf{p}_e / \mid\mid \mathbf{p}_e \mid\mid) \mathcal{F}\Big(\frac{\omega}{\omega_{cr}}\Big) \tag{A.1}$$

The delta function in equation (A.1) ensures that the radiation is primarily emitted along the direction of the electron momentum, $\mathbf{p}_e$. The critical frequency, ω_{cr} is defined by the electron oscillation frequency in the external fields. Synchrotron radiation is typically described in terms of the motion of an electron in a constant magnetic field, in which case the critical frequency is related to the electron oscillation frequency, $\omega_r = \mid \mathbf{p}_e \times \mathbf{F}_{L,e} \mid / p_e^2$, by the expression $\omega_{cr} = \frac{3}{2}\omega_r \gamma_e^2$. In the case of electron motion in strong fields, this oscillation frequency is replaced with the laser frequency. $\mathcal{F}(\omega/\omega_{cr})$ is the MacDonald function which describes the shape of the emitted spectrum and is defined as $\mathcal{F}(\omega/\omega_{cr}) = \frac{9\sqrt{3}}{8\pi}\frac{\omega}{\omega_{cr}}\int_{\omega/\omega_{cr}}^{\infty} K_{5/3}(x)dx$, where $K_{5/3}$ is a modified Bessel function [16, 17].

Appendix A.2. Accounting for quantum effects

The Landau-Lifshitz (LL) equation provides a classical description of RR, in which quantum corrections to the electron trajectory, and pair-production, are neglected. The importance of such quantum effects are quantified by the Lorentz invariant parameter, χ_e:

$$\chi_e = \frac{\gamma_e}{eE_{sh}} \sqrt{\mathbf{F}_{L,e}^2 - (\mathbf{F}_{L,e} \cdot \boldsymbol{\beta})^2} \tag{A.2}$$

where E_{sh} is the Schwinger limit for electric field strength, such that $E_{sh} = m_e^2 c^3 / e\hbar$ [22]. The χ_e parameter is the ratio of the electric field strength experienced by an electron in its rest frame compared to the Schwinger limit. Hence, when $\chi_e \simeq 1$, the electron experiences an electric field strength in its rest frame which is comparable to that of the Schwinger field, leading to a non-negligible pair production rate.

The classical approach described by the LL equation overestimates the electron radiated power, as it does not account for the probabilistic nature of photon emission. The resulting stochastic effects are described in further detail in references [47, 48, 49, 50] and can be accounted for by introducing a scaling function, $g(\chi_e)$, to the RR term in the LL equation. This scaling reduces the electron radiated power and consequently the amplitude of the RR force. The appropriate scaling function is defined in references [51, 52] as $g(\chi_e) = (3.7\chi_e^3 + 31\chi_e^2 + 12\chi_e + 1)^{-4/9}$.

The stochastic effects described here become important for values of $\chi_e \gtrsim 0.1$, where the radiated power is reduced by a factor of 2/3. However, it has been demonstrated in references [51, 53, 54] that the stochastic effects do not affect the average energy loss of the electrons, which is the most important consideration for the model presented in this paper.

In ultra-intense laser solid interactions, the electrons which obtain the highest χ_e values and therefore experience the strongest RR force, are those which counter-propagate against the laser pulse [55]. Since the electron velocity is oriented opposite to the laser propagation direction, the electron experiences Doppler upshifting of the laser fields in its rest frame and consequently a higher χ_e, stimulating strong radiation emission. The radiative cooling of these electrons prevents them from propagating against the laser pulse and they are reflected, becoming trapped at the laser plasma interface. The effects of the trapped electron population have been investigated in references [28, 29, 24, 56, 57].

Appendix A.3. The Maxwell Juttner distribution

In section 3, we assume that the electron distribution function can be modelled using a Maxwell Juttner (or relativistic Maxwell) distribution. Although this distribution is collisional, whilst the simulations we present are collisionless, it is found to be a good fit to the electron spectra. This is demonstrated in figure A1, where the electron energy spectra are compared for a 400 nm target, with and without RR. The spectra are measured at times $t = 40\ T_L$, which is the maximum radiation emission time, $t = 45\ T_L$ and $t = 50\ T_L$.

Figure A1 demonstrates that RR causes cooling of the electron spectra, relaxing the system towards an equilibrium distribution. This is analogous to the cooling of electrons through binary collisions in a collisional system. Finally, a Maxwell Juttner distribution is required as opposed to a pure Maxwell distribution, since the electrons are heated to relativistic velocities by the oscillating component of the laser ponderomotive

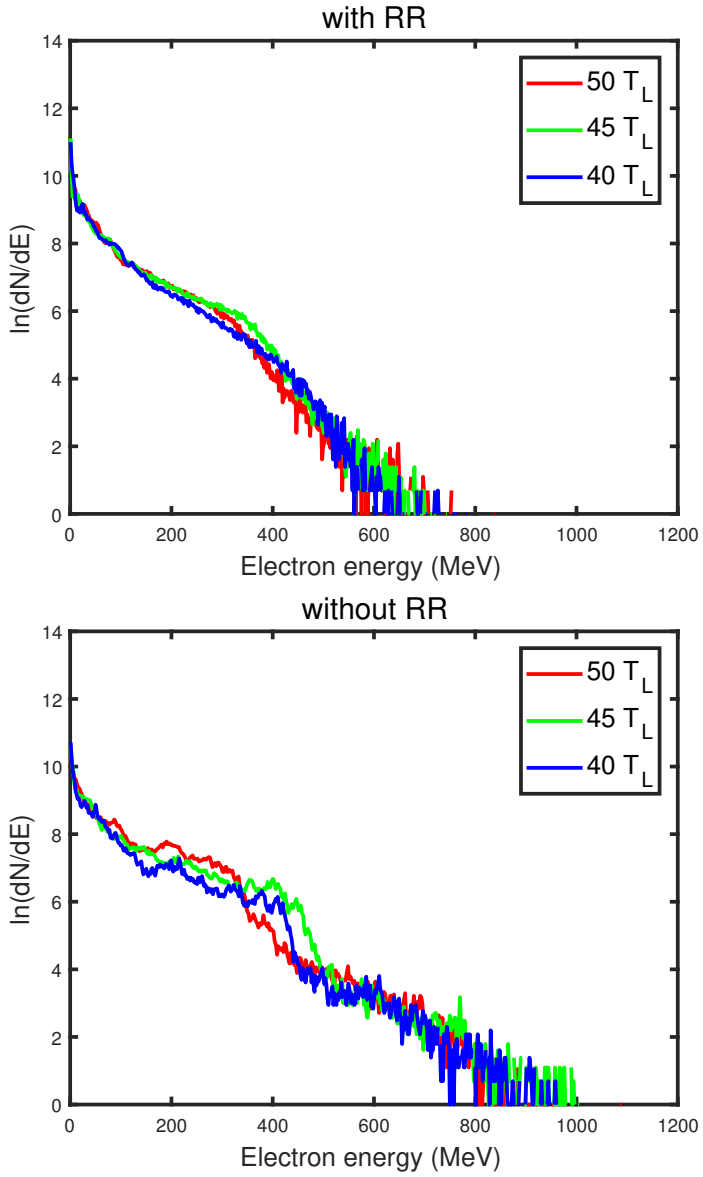

Figure A1. Electron energy spectra measured from a 400 nm target at times $t = 40\,T_L$ (blue line, corresponding to the maximum radiation emission time), $t = 45\,T_L$ (green line) and $t = 50\,T_L$ (red line). The top panel is the case with RR on, whilst the bottom panel has RR off.

force.

References

[1] Habs D, Tajima T and Zamfir V 2011 *Nuclear Physics News* **21** 23-29

[2] Zou J, Le Blanc C, Papadopoulos D, Cheriaux G, Georges P, Mennerat G, Druon F, Lecherbourg L, Pellegrina A, Ramirez P *et al.* 2015 *High Power Laser Science and Engineering* **3** e2

[3] Ji L, Pukhov A, Nerush E, Kostyukov I Y, Shen B and Akli K 2014 *Physics of Plasmas* **21** 023109

[4] Liseykina T V, Borghesi M, Macchi A and Tuveri S 2008 *Plasma Physics and Controlled Fusion* **50** 124033

[5] Weng S, Lui M, Sheng Z, Murakami M, Chen M, Yu L and Zhang J 2016 *Scientific Reports* **6**

[6] Esirkepov T, Borghesi M, Bulanov S, Mourou G and Tajima T 2004 *Physical review letters* **92** 175003

[7] Bulanov S and Khoroshkov V 2002 *Plasma Physics Reports* **28** 453-456

[8] Roth M, Cowan T E, Key M H, Hatchett S P, Brown C, Fountain W, Johnson J, Pennington D M, Snavely R A, Wilks S C, Yasuike K, Ruhl H, Pegoraro F, Bulanov S V, Campbell E M, Perry M D and Powell H 2001 *Physical Review Letters* **86**(3) 436-439

[9] Pukhov A 2002 *Report on progress in Physics* **66** 47

[10] Macchi A, Borghesi M and Passoni M 2013 *Rev. Mod. Phys.* **85**(2) 751793

[11] Yin L, Albright B J, Bowers K J, Jung D, Fernandez J C and Hegelich B M 2011 *Physical Review Letters* **107**(4) 045003

[12] Henig A, Kiefer D, Markey K, Gautier D C, Flippo K A, Letzring S, Johnson R P, Shimada T, Yin L, Albright B J, Bowers K J, Fernandez J C, Rykovanov S G, Wu H C, Zepf M, Jung D, Liechtenstein V K, Schreiber J, Habs D and Hegelich B M 2009 *Phys. Rev. Lett.* **103**(4) 045002

[13] Powell H, King M, Gray R, MacLellan D, Gonzalez-Izquierdo B, Stockhausen L, Hicks G, Dover N, Rusby D, Carroll D *et al.* 2015 *New Journal of Physics* **17** 103033

[14] Di Piazza A, Hatsagortsyan K Z and Keitel C H 2009 *Physical Review Letters* **102**(25) 254802

[15] Dirac P A 1938 *Proceedings of the Royal Society of London. Series A, Mathematical and Physical Sciences* 148169

[16] Landau L D and Lifshitz E M 2000 The classical theory of fields: Volume 2 (course of theoretical physics series)

[17] Jackson J D 1999 Classical electrodynamics

[18] Dinu V, Harvey C, Ilderton A, Marklund M and Torgrimsson G 2016 *Physical review letters* **116** 044801

[19] Wistisen T N, Di Piazza A, Knudsen H V and Uggerhj U I 2017 *ArXiv e-prints (Preprint 1704.01080)*

[20] Cole J M, Behm K T, Blackburn T G, Wood J C, Baird C D, Duff M J, Harvey C, Ilderton A, Joglekar A S, Krushelnik K, Kuschel S, Marklund M, McKenna P, Murphy C D, Poder K, Ridgers C P, Samarin G M, Sarri G, Symes D R, Thomas A G R, Warwick J, Zepf M, Najmudin Z and Mangles S P D 2017 *ArXiv e-prints (Preprint 1707.06821)*

[21] Poder K, Tamburini M, Sarri G, Di Piazza A, Kuschel S, Baird C D, Behm K, Bohlen S, Cole J M, Duff M, Gerstmayr E, Keitel C H, Krushelnick K, Mangles S P D, McKenna P, Murphy C D, Najmudin Z, Ridgers C P, Samarin G M, Symes D, Thomas A G R, Warwick J and Zepf M 2017 *ArXiv e-prints (Preprint 1709.01861)*

[22] Schwinger J 1951 *Physical Review* **82**(5) 664679

[23] Nerush E and Kostyukov I Y 2015 *Plasma Physics and Controlled Fusion* **57** 035007

[24] Capdessus R and McKenna P 2015 *Physical Review E* **91** 053105

[25] Macchi A, Veghini S and Pegoraro F 2009 *Physical review letters* **103** 085003

[26] Macchi A, Veghini S, Liseykina T V and Pegoraro F 2010 *New Journal of Physics* **12** 045013

[27] Levy M, Wilks S, Tabak M and Baring M 2013 *Physics of Plasmas* **20** 103101

[28] Chen M, Pukhov A, Yu T P and Sheng Z M 2010 *Plasma Physics and Controlled Fusion* **53** 014004

[29] Tamburini M, Pegoraro F, Di Piazza A, Keitel C H and Macchi A 2010 *New Journal of Physics*

12 123005
[30] Cherepenin V A and Kulagin V V 2004 *Physics Letters A* **321** 103110
[31] Umstadter D 2003 *Journal of Physics D: Applied Physics* **36** R151
[32] Erber T 1966 *Reviews of Modern Physics* **38** 626
[33] Krivitskii V and Tsytovich V N 1991 *Soviet Physics Uspekhi* **34** 250
[34] Ilderton A and Torgrimsson G 2013 *Physics Letters B* **725** 481486
[35] Del Sorbo D, Blackman D R, Capdessus R, Small K, Slade-Lowther C, Luo W, Duff M J, Robinson A P L, McKenna P, Sheng Z M, Pasley J and Ridgers C P 2017 *ArXiv e-prints (Preprint 1706.04153)*
[36] Capdessus R, dHumieres E and Tikhonchuk V 2013 *Physical Review Letters* **110** 215003
[37] Capdessus R, King M and McKenna P 2016 *Physics of Plasmas* **23** 083117
[38] Liseykina T, Popruzhenko S and Macchi A 2016 *New Journal of Physics* **18** 072001
[39] Simmons J and McInnes C 1993 *American journal of physics* **61** 205207
[40] Baier V and Katkov V 1968 *Sov. Phys. JETP* **26** 854
[41] Arber T, Bennett K, Brady C, Lawrence-Douglas A, Ramsay M, Sircombe N, Gillies P, Evans R, Schmitz H, Bell A et al. 2015 *Plasma Physics and Controlled Fusion* **57** 113001
[42] Di Piazza A, Hatsagortsyan K and Keitel C H 2010 *Physical review letters* **105** 220403
[43] Turcu I, Negoita F, Jaroszynski D, Mckenna P, Balascuta S, Ursescu D, Dancus I, Cernaianu M, Tataru M, Ghenuche P et al. 2016 *Romanian Reports in Physics* **68** S145S231
[44] Robinson A, Gibbon P, Zepf M, Kar S, Evans R and Bellei C 2009 *Plasma Physics and Controlled Fusion* **51** 024004
[45] Capdessus R, Lobet M, dHumieres E and Tikhonchuk V 2014 *Physics of Plasmas* **21** 12312
[46] Schlenvoigt H P, Haupt K, Debus A, Budde F, Jackel O, Pfotenhauer S, Schwoerer H, Rohwer E, Gallacher J, Brunetti E *et al.* 2008 *Nature Physics* **4** 130133
[47] Neitz N and Di Piazza A 2013 *Physical review letters* **111** 054802
[48] Duclous R, Kirk J G and Bell A 2010 *Plasma Physics and Controlled Fusion* **53** 015009
[49] Blackburn T, Ridgers C, Kirk J G and Bell A 2014 *Physical review letters* **112** 015001
[50] Kirk J G, Bell A R and Arka I 2009 *Plasma Physics and Controlled Fusion* **51** 085008
[51] Ridgers C, Kirk J G, Duclous R, Blackburn T, Brady C, Bennett K, Arber T and Bell A 2014 *Journal of Computational Physics* **260** 273285
[52] Ridgers C P, Blackburn T G, Del Sorbo D, Bradley L E, Baird C D, Mangles S P D, McKenna P, Marklund M, Murphy C D and Thomas A G R 2017 *ArXiv e-prints (Preprint 1708.04511)*
[53] Ridgers C *et al* 2017 *Journal of Plasma Physics* **83**
[54] Niel F, Riconda C, Amiranoff F, Duclous R and Grech M 2017 *ArXiv e-prints (Preprint 1707.02618)*
[55] Brady C S, Ridgers C, Arber T, Bell A and Kirk J 2012 *Physical review letters* **109** 245006
[56] Ji L, Pukhov A, Kostyukov I Y, Shen B and Akli K 2014 *Physical review letters* **112** 14500
[57] Gonoskov A, Bashinov A, Gonoskov I, Harvey C, Ilderton A, Kim A, Marklund M, Mourou G and Sergeev A 2014 *Physical review letters* **113** 014801